

Multi-wavelength analysis of Ly α -emitting high-redshift galaxies

Master's Thesis Spring 2004
Kim Nilsson
Lund Observatory, Lund University
Thesis supervisors:
Kristian Pedersen,¹
Johan P.U. Fynbo,^{1,2}
Ingemar Lundström³
& Melvyn B. Davies³

¹Niels Bohr Institute, Copenhagen Astronomical Observatory, Denmark

²Department of Physics and Astronomy, University of Århus, Denmark

³Lund Observatory, Lund University, Sweden

Contents

1	Introduction	3
2	Theory	6
2.1	High-redshift galaxies	6
2.2	Ly α theory	9
2.3	X-ray theory	10
2.3.1	What causes X-rays?	11
2.3.2	What is an AGN?	12
2.3.3	Star Formation Rate	14
2.3.4	Classifying an X-ray source	19
2.4	Infrared theory	20
3	Sample, method and results	22
3.1	Ly α sample	22
3.1.1	Coordinate transformation	22
3.1.2	Luminosity of Ly α -sources	23
3.2	X-ray sample	24
3.2.1	CXO, Chandra Deep Field South and GOODS	24
3.2.2	Measurements and results	26
3.2.3	Error calculation and randomness	29
3.3	Infrared and optical sample	30
3.3.1	ISAAC	30
3.3.2	ISAAC measurements and results	30
3.3.3	Visual broad band measurements	31
3.4	Radio counterparts	31
4	Discussion	33
5	Summary	39
A	Spectral Energy Distributions	40

Chapter 1

Introduction

Purpose

The purpose of this Master's Thesis is to perform a multi-wavelength analysis of 15 Ly α -bright galaxies, at redshift 3.2, in the GOODS Field South. Observations in X-rays and infrared have been studied. We have been especially interested in investigating whether X-ray fluxes are detectable from these galaxies under the assumption that the X-ray fluxes are powered by either X-ray binaries, which is a measure of star formation, or non-thermal processes related to the central black hole in faint active galactic nuclei, AGN. We have also attempted to find the star formation rate of the galaxies from the X-ray fluxes and the flux in Ly α emission.

General framework of this study

The aim of studies of how and when galaxies form is to gain insight into how the Universe evolved from the very homogeneous state probed by the Cosmic Microwave Background to the very structured Universe of galaxies and stars we see today. Galaxies may be considered the main building blocks of large scale structure, and constitute themselves some of the largest bound structures in the Universe. Because of the fundamental role galaxies play in the Universe, understanding how they form is of central importance to extra-galactic astronomy. The current cosmological models used are mainly based on the cold dark matter model and the spectrum of initial density perturbations from inflation. By observing the properties of the first galaxies we put this model to the test.

The desire to study galaxy formation in the distant Universe goes back to the 60's. However, it has only been possible during the last 10 years or so, to locate such very distant galaxies on the sky (except AGN that are galaxies completely dominated by emission from their central black holes). Today there are a handful of available methods by which to locate

such young galaxies: *i*) absorption methods, *ii*) broad band colours, *iii*) narrow band emission techniques, *iv*) sub-mm emission from cold dust in starbursts, and *v*) gamma-ray burst selection (of the galaxies hosting the bursts). These methods are discussed in detail in section 2.1.

To better understand the high-redshift galaxies themselves, several questions need to be answered. Some of them are:

- What is the volume density of galaxies/AGNs at high-redshift?
- What mechanisms drive these galaxies?
- How many stars are forming and how does that influence the star formation history?
- When did the first galaxies form?

These are the types of questions that set the background for this study.

Wavelength regions

The electromagnetic spectrum consists of seven large wavelength intervals, in descending order of energy: gamma rays, X-rays, ultraviolet, visual, infrared and radio. The widths of these intervals vary, and some are subdivided, e.g. hard/soft X-rays or near/far infrared. In this study, the galaxies are observed in the three wavelength regions: X-rays, visual and (near-) infrared. These regions are the *observed* ones and correspond to X-rays, UV and visible in the restframe of the galaxies. The reasons for choosing these regions are partly the availability of deep observations, and partly that they trace interesting processes. X-rays can trace either AGN or X-ray binaries, UV trace star formation because it is emitted by newborn stars and visual light is a measure of the stellar mass of the galaxy. Special effort is spent on the emission in Ly α , because this is the distinguishing property of the sources. The Ly α luminosity can easily be converted to a star formation rate, SFR, i.e. number of solar masses created per year in a galaxy. Also, one of the galaxies show very extended Ly α emission, a so-called “blob”. This emission is believed to come from either a strong stellar wind from new stars, or from a large cloud of hydrogen that is cooling. The theory behind this is discussed in section 2.2. To some extent, the radio region is also covered, by searching for radio counterparts in several databases. The results from those investigations can be found in section 3.4.

This study has been made in collaboration with Copenhagen University, from where the two main supervisors come. The outline of the thesis is

that the theory that precedes the observations, as well as some general theory relevant to the thesis, is described in Chapter 2, an outline of the measurements and results are in Chapter 3 and a discussion and conclusion can be found in Chapter 4. Chapter 5 holds a summary. Unless stated otherwise, it is everywhere assumed that $H_0 = 65 \text{ km s}^{-1} \text{ Mpc}^{-1}$, $\Omega_M = 0.3$ and $\Omega_\Lambda = 0.7$. At redshift 3.2 the luminosity distance¹ is $9.128 \cdot 10^{28} \text{ cm} = 29600 \text{ Mpc}$ and the angular diameter distance, meaning what the proper, rest-frame distance one arcsecond on the sky corresponds to, is $8.13 \text{ kpc/arcsecond}$. The look-back time² is 12.4 Gyrs. All magnitudes in this thesis are, unless stated otherwise, AB magnitudes.

¹The luminosity distance can be calculated using the formula: $d_L = (1+z)r$ where z is the redshift, a the scale factor and r the proper distance.

²The look-back time can be calculated from the formula:

$$\Delta t = H_0^{-1} \int_0^{z_1} (1+z)^{-1} [(1+z)^2(1+\Omega_M z) - z(2+z)\Omega_\Lambda]^{-1/2} dz$$

Chapter 2

Theory

This theory chapter is divided into four sections covering how to find high-redshift galaxies and the three major wavelength regions studied. The X-ray section is then subdivided into four subsections that firstly deal with the origin of X-rays. Next, two subsections on what we might expect to see, AGNs or a collection of X-ray binaries. Finally a subsection on how one might discern between an AGN or X-ray binaries.

2.1 High-redshift galaxies

What is redshift?

I have studied the star formation and general properties of galaxies at a high redshift. Redshift is a measure of how far away in space an object lies and also how far back in time we observe it, because light travels with a limited speed, so looking further away also means looking at light that left that object a specific time ago. The cosmological redshift measures how much the universe has expanded between the emission of radiation from the source, and its subsequent observation by telescopes on Earth. The redshift follows the equation:

$$1 + z = \frac{a(t_{obs})}{a(t_{em})} \quad (2.1)$$

where $a(t_{obs})$ and $a(t_{em})$ are the respective values of the scale factor at the time of observation and emission. The formulation of the scale factor depends on the cosmological model chosen, and given for instance a Friedmann model the look-back time and proper distance corresponding to a certain redshift can be calculated. This can be done using one of many "cosmic calculators" found on Internet¹. For a more extensive

¹For instance <http://www.astro.ku.dk/~brian-j/cc>

description of redshift and cosmological models, the reader is referred to e.g. Ryden (2003).

Why are we interested in what happens at large redshift? It is interesting to find how the galaxies formed, and also what amount of stars formed at what time. Galaxies formed a long time ago, and looking at high-redshift galaxies means observing the galaxies when they were very young. The amount of stars forming is described by the star formation rate, SFR. SFR is measured in number of solar masses created per year. There are several indicators of this number. The two studied here are the luminosity of the object in X-rays and Ly α . The connection between Ly α emission and formation of stars is the de-excitation of the surrounding medium, that has been excited by UV-light from newborn stars. More stars forming \rightarrow more UV-light \rightarrow more excitation/de-excitation \rightarrow more emission. The connection X-ray luminosity - SFR comes from assuming that the X-ray flux is dominated by X-ray binaries. An X-ray binary is a binary in which one of the stars has evolved into a neutron star and is accreting material from the companion. When more stars are formed, more will evolve into neutron stars and hence more X-ray binaries will appear. This connection is explained in greater detail in section 2.3.3.

How can we examine what happens at high redshift? Since the galaxies studied in this thesis are at a very large distance from us, the light will be very redshifted. Thus, if we are looking at a certain wavelength in the restframe of the galaxy, the wavelength in our telescope will be larger than this. The redshift is linearly proportional to the wavelength, so a longer restframe wavelength means a much longer observed wavelength. Because of this it can be convenient to study objects at shorter wavelengths. X-rays are very useful because they tell us something about the character of the galaxy, for instance reveal the presence of an AGN, based on the luminosity and spectral characteristics. X-rays can also probe ongoing star formation by means of X-ray binaries. Other intervals are of interest, one of which is the region around the Ly α line in the rest frame, since this has a close connection to the SFR. The infrared regions, which means near-UV at redshift 3.2, is interesting because it reflects the amount of stellar matter in the galaxy. There may also be a reason to look for radio counterparts, because its presence can confirm that the galaxy harbours an AGN. Of course, choosing in what wavelength region to observe is also a question of opportunity, because there are physical and temporal constraints. Physical constraints are that certain wavelength regions can be difficult to observe, for instance gamma-rays are difficult to focus and need to be observed from space. A temporal constraint is that getting observing time at a telescope is a long procedure from submission of proposal to acceptance to actual observation. That time is not available to me during the work of this thesis.

How to find them

The method for finding the high-redshift galaxies used here is based on the Ly α emission from the galaxy. But there are several ways of finding these distant galaxies. I will briefly explain the main methods. The five methods used today are:

- Absorption technique
- Lyman-break technique
- Lyman-emission technique
- Sub-mm surveys
- Gamma-ray bursts

The first uses the great luminosity of distant quasars to spot objects situated between the quasar and us in the line of sight. Such an object will cause absorption lines in the spectra of the quasar. Identification of the line will give the redshift and hence the distance. One class of such systems are Damped Ly α Absorption (DLA) systems. The advantage of this method is that they are easily found. The disadvantage is that the objects are always situated near a bright quasar along the line of sight and extended investigations in multiple wavelength regions are complicated, due to saturation of the background source.

The second method is the most extensively used, the Lyman-break method. Hydrogen is ionised at a wavelength $\lambda \leq 912 \text{ \AA}$. Because of the great amount of hydrogen in the universe, most of the light more energetic than this “Lyman-limit”, will be absorbed and there is a large intensity drop in the spectrum of a galaxy. When the galaxy lies at large redshift, this break is shifted into the optical regime and by using photometry, with broad bands placed on either side of this intensity drop, one can find its approximate redshift. This is a “cheap” way of finding high-redshift galaxies, but the disadvantages are that there may be other reasons for an intensity drop, such as dust obscuration, and often spectroscopic follow-ups are needed to confirm the redshift, although the contamination due to low-redshift galaxies is small. A full description of the method can be found in Steidel *et al.* (2003).

The third method, used here, looks for the Ly α spectral line in very narrow filters matching the redshift of the source, see section 2.2. The galaxies found to be luminous in the narrow filter are well determined to correspond to the redshift of the Ly α line at the filter wavelength position. Draw-backs are that the emission line peaking in the filter could be another line than Ly α , from a galaxy at a different redshift, for instance [OII] at restframe $\lambda = 3727 \text{ \AA}$ or CIV with restframe $\lambda = 1551 \text{ \AA}$.

This effect is however not very large, the confirmation rate in the Building the Bridge survey of Fynbo *et al.* (2003) (in which the sources studied here were found) is about 70 % or larger.

Sub-mm galaxies are galaxies that are very bright in the far-IR and appear to be highly dust obscured star forming galaxies. Dust absorbs the light from the young stars and is heated to typically a few ten K, corresponding to a maximum in intensity in sub-mm wavelengths according to Wiens displacement law. A large number of such sources have been found by the SCUBA (Sub-mm Common User Bolometer Array), see e.g. Ivison *et al.* (2002). However, most of them are very faint at other wavelengths and are therefore difficult to study.

Finally, the use of gamma-ray bursts have revealed very faint galaxies at high-redshift. It is believed that these, extremely energetic, bursts are the result of a special sort of supernova. When they appear, the luminosity of the object increases greatly, mostly in gamma-rays, but most also have an x-ray/optical/radio afterglow that makes it possible to get a spectroscopic confirmation of the redshift of the host galaxy. The problem is locating the positions of these bursts and understanding the mechanism behind them.

The great problem in research about high redshift galaxies is the poor understanding of gamma-ray bursts and the biases to each of the methods mentioned here. It is necessary to study each method, in order to get a complete understanding of what the Universe looks like at high redshift.

2.2 Ly α theory

Hydrogen is the overwhelmingly most abundant element in the universe, as much as 90 % of all atoms are hydrogen atoms. Thus, hydrogen spectral lines are strong and pronounced in stellar, as well as galactic, spectra. This makes hydrogen a valuable tool, especially in determining the redshifts of distant galaxies. So far, the dominating method of finding high-redshift galaxies and quasars have been the Lyman-break method, see section 2.1. In the method used to find the sources studied here, the Ly α spectral line is searched for in emission. By comparing the intensity in a narrow filter, targeting the Ly α -emission, with broad band filters on either side of the narrow filter, and plotting a colour-colour diagram, one can determine which objects are at the particular redshift corresponding to the narrow filter. Ly α luminous high-redshift galaxies will be more luminous in the narrow filter, than in the broad band filters. The method has been proved successful, and is described in detail in Fynbo *et al.* (2003). This is, as already mentioned, the method used to find the 15 sources studied here, which were found at redshift 3.2.

One of the sources, Source # 9, is very extended ($\sim 4'' = 33$ kpc in

the restframe), a so-called “blob”. Such blobs have also been found by others, e.g. Steidel *et al.* (2000). The origin of these blobs is unknown, but there are some theories. Steidel *et al.* (2000) present the theory that the blobs could be created by a cooling gas, a so-called “cooling flow”. A cooling flow happens when gas in e.g. a galaxy cluster emit such a large amount of energy in the form of X-rays that it cools. If the collection of gas is smaller, e.g. the size of a galaxy, the energy can be lost as UV-light. Any gas that cools will contract due to pressure loss, hence the term “flow”. Such a contraction will cause a build-up of cool gas in the center of the region, where star formation may be facilitated. A second theory Steidel *et al.* (2000) mention is that there might be continuum sources, hidden to us, ionising the surroundings that will scatter Ly α emission in our direction. Of course, they also consider star formation as an origin of the blobs, but the large star formation rates implied ($> 160 M_{\odot}/\text{yr}$) speaks against the theory. More likely values of the SFR of these galaxies are some ten M_{\odot}/yr , e.g. a study by Reddy & Steidel (2004) find $\sim 70 M_{\odot}/\text{yr}$ in galaxies with similar redshifts. In another paper by Ohyama *et al.* (2003) the blobs from the paper by Steidel *et al.* (2000) are revisited. They consider two possible origins: a “superwind” from galactic outflow due to extreme star formation or the cooling flow theory. To separate between the models, Ohyama *et al.* (2003) study the velocity broadening of the emission lines which will be different in the two models. Their results favour the superwind theory.

2.3 X-ray theory

Now for the theory of X-rays. X-rays are commonly known as a practical tool in medicine, to see the inside of a human without opening her up, because X-rays can penetrate deep into tissue, and other less dense materials without causing too much damage on the way. This is also an excellent quality when looking “deep” into the universe. X-rays are created in places where violent processes are occurring, because of the energetic nature of the radiation, and the most energetic photons can penetrate dust and gas surrounding this site and travel all the way to us. Generally, the energy of X-rays is measured in keV and covers the range $\sim 0.1 - 100$ keV. Less energetic photons are classified as ultra-violet and more energetic as gamma-rays. In fact, X-rays are particularly useful in finding active galaxies (star forming active to some extent, but mostly AGN). Surveys in X-rays have discovered a larger number of quasars than surveys in optical bands (Mushotzky *et al.* 1993) and the rapid variations in the X-ray luminosity of some quasars indicate that the radiation is emanating from a small volume close to the source. This means that the X-rays can be used as probes to investigate the core regions of AGNs.

2.3.1 What causes X-rays?

X-rays can be generated in several ways. Some of the main sources are:

- Bremsstrahlung
- Synchrotron radiation
- Blackbody/Thermal radiation

The first, bremsstrahlung, comes from interactions between free electrons and positive ions in a plasma. An electron passing close to an ion will bend its trajectory, due to electric forces. This will accelerate the electron, causing it to send out electromagnetic radiation. The spectrum of this bremsstrahlung will be dependent on the temperature of the plasma, and at temperatures higher than ~ 1 million Kelvin, this radiation will be mainly in X-rays. The intensity of the radiation, as a function of energy, E , and temperature, T , of the plasma is:

$$I(E, T) \propto Z^2 n_e n_i (kT)^{-1/2} e^{-E/kT} \quad (2.2)$$

where Z is the charge of the positive ions and n_e and n_i the electron and positive ion density. All equations in this subsection are taken from Charles & Seward (1995).

Synchrotron radiation is similar to bremsstrahlung in the sense that it is created when the path of an electron is bent. But with synchrotron radiation the electron is spinning in a magnetic field, because the force on an electron is the scalar product of the velocity of the electron and the direction of the magnetic field. The force will cause the electron to spin around the magnetic field lines, and it will be accelerated. The spectrum for synchrotron radiation follows a power law:

$$I(E) = N E^{-\Gamma} \quad (2.3)$$

Here N is a constant and Γ the photon index. We will later assume a power law for our measurements.

The third way to get X-rays is from very hot, blackbody radiating objects. A blackbody radiator is an object that absorbs all light incident on it and radiate the equivalent energy in a smooth spectrum, that is only dependent on the temperature of the object. The spectra of stars are nearly blackbody shaped, with emission/absorption lines overlaid. When the temperature of the object reaches 1 million Kelvin or greater, the peak of the spectrum lies in X-rays. The intensity will in this case equal the following formula:

$$I(E, T) = 2E^3 [h^2 c^2 (e^{E/kT} - 1)]^{-1} \quad (2.4)$$

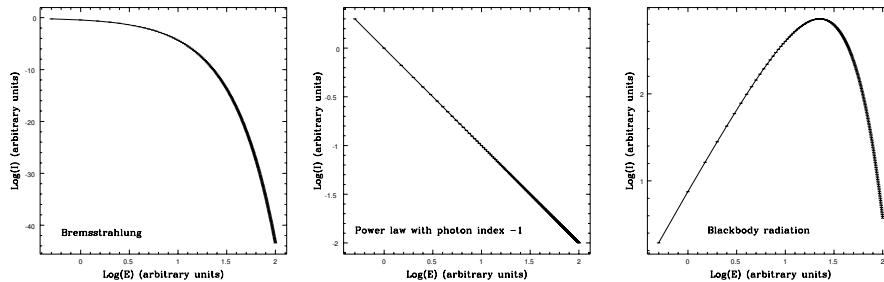


Figure 2.1: Schematic spectra of the three main X-ray causes. On the x-axis we find $\log(E)$ and on the y-axis $\log(I)$. The axes have arbitrary units.

Simple schematic plots of the spectra of these three main sources of X-rays can be found in Fig. 2.1.

A fourth possibility is inverse Compton scattering. Compton scattering means that an energetic photon can transfer its energy to an atomic electron that will be expelled from the atom. Inverse Compton radiation will conversely mean that an energetic electron will interact with a low-energy photon and transfer energy.

The assumption of a power law for the X-ray spectrum is of relevance (in this thesis) only when calculating counts to flux and there are three major reasons to why we choose it. First, a power law is the most simple analytical model possible, and it is convenient as a first approximation to use the simplest model. Secondly, several studies of X-ray spectra from the same type of objects have revealed a power law spectra. Thirdly, both AGNs and X-ray binaries, XRBs (see section 2.3.3), have power law spectra individually, and because we assume to see either an AGN or a large number of XRBs or both we can easily justify that any X-ray spectra we see will, to a first approximation, follow a power law.

2.3.2 What is an AGN?

The name AGN (Active Galactic Nuclei) came from early observations of galaxies where the nuclei outshone the entire galaxy. In fact, AGNs were first recognized as powerful radio sources. Only later were they tied to optical counterparts with redshifted spectra. When investigations of the sky in X-rays started in the 60's, it was discovered that just about all AGNs also emitted strongly in these wavelength regions.

The basic property of an AGN is the enormous luminosity. The comparable X-ray luminosity of galaxy-type objects in our Universe can be found in Table 2.3.2, numbers from Charles & Seward (1995) and Norman *et al.* (2004). In a normal galaxy, the X-rays come from XRBs and

supernova remnants. In AGNs, from non-thermal processes associated with the accretion onto a central black hole.

Type	L_x (erg s ⁻¹)
Normal galaxy	$10^{37} - 10^{42}$
Seyfert galaxy	$10^{40} - 10^{45}$
Quasar	$10^{45} - 10^{47}$

The morphology is different in an AGN or a normal galaxy. A galaxy is a much larger, extended object while an AGN is a smaller, compact object. AGNs are usually embedded in a galaxy.

There are many names and classifications for these types of objects, but according to the present theory, called the “unifying theory”, all emanate from the same kind of objects, seen at different angles and directions. The basic idea is that all AGNs have a very massive black hole in its centre and some form of accretion disk, off which it is feeding. The potential energy of the material orbiting the black hole is released when material is accreted. The energy released follows the seemingly simple equation:

$$\dot{E} = \frac{GM}{R} \cdot \dot{M} \quad (2.5)$$

where \dot{E} is the rate of change of the energy, which is basically luminosity. The fraction on the left hand side is the potential of the matter in the accretion disk and \dot{M} is the change of mass in the accretion disk. However, equation 2.5 is not as simple as it looks. The \dot{M} term can be difficult to calculate. The Eddington luminosity is the greatest luminosity an object of a certain mass can have. If the mass becomes greater, due to accretion, the luminosity will increase and the number of photons that are sent out will be greater. These photons will in turn be scattered off the material falling onto the object, transferring momentum, and the accreting material will be diverted, i.e. the mass accretion will stop. The Eddington luminosity can be found to be, when balancing the radiation pressure with the gravitational force:

$$L_{Edd} = 1.3 \cdot 10^{38} (M/M_{\odot}) \text{ erg s}^{-1} \quad (2.6)$$

Thus, a black hole with mass $\sim 10^8 M_{\odot}$ will have a greatest luminosity of about $10^{46} \text{ erg s}^{-1}$. A schematic image of the unified AGN model can be seen in Fig 2.2. Here we see the central black hole with a small accretion disk surrounding it. Jets are beamed in opposite directions from the poles of the black hole, presumably collimated by magnetic fields surrounding the black hole. Some distance from the centre lies a large molecular torus and also clouds of atoms and molecules that create, depending on distance

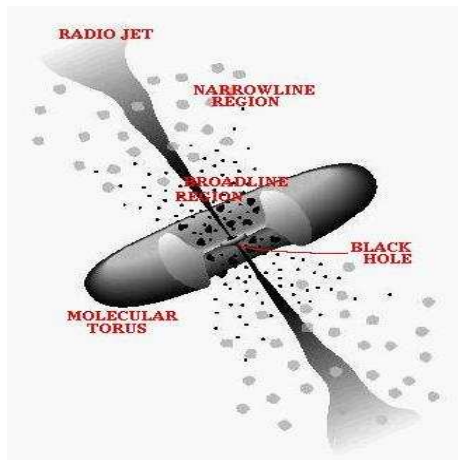


Figure 2.2: Schematic drawing of a the unified theory of AGNs. From Urry and Padovani 1995.

from the black hole, broad or narrow emission lines. Broad lines when we observe clouds located very close to the actual black hole that have high velocity broadening, and narrow when we see the clouds surrounding the nuclei at a greater distance. According to the theory, all classifications of active galaxies can be derived from this model. Blazars are objects where we see straight into the jets. Seyfert 1 galaxies, or type 1 AGNs are objects where we look at an angle in between the jets and the torus, and Seyfert 2s/type 2 AGNs are objects where the central source is obscured by the molecular torus.

The most obvious spectral feature that dominates the continuum of an AGN is “the big blue bump”, extending from 4000 \AA to short-ward wavelengths, possibly all the way to the X-ray region. As discussed in section 2.3.4, this bump comes from the accretion disk surrounding the central black hole. An example of the spectrum of an AGN in the UV/optical region can be found in Fig. 2.3.

2.3.3 Star Formation Rate

What is star formation rate?

The star formation rate (SFR) is the number of stars formed during an interval of time, and is usually measured in M_{\odot}/yr per galaxy. It is interesting to study how this SFR has changed over time. Before $z \sim 6$ the universe was dark, with no or few stars present². It was after this

²There is debate over the exact redshift when galaxies formed, with the recent press release of a $z = 10$ galaxy, Pelló *et al.* (2004). This has not been confirmed yet, and

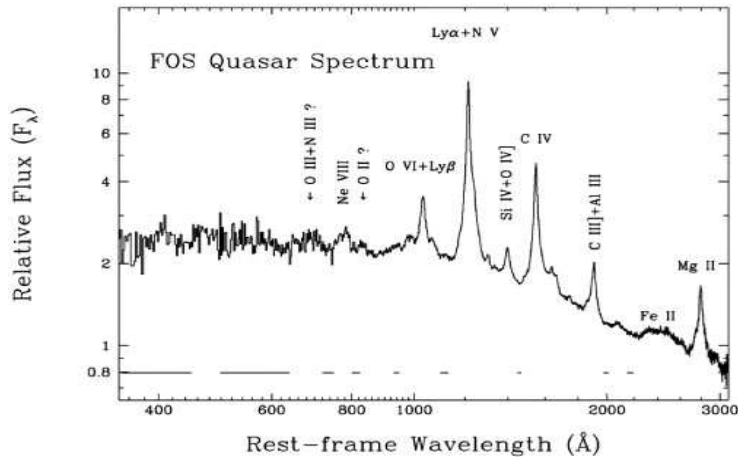


Figure 2.3: Composite spectrum of 101 quasars. From Zheng *et al.* (1997).

that galaxies formed. The SFR of our galaxy, the Milky Way, is presently $\sim 3 M_{\odot}/\text{yr}$ (Smail (2002)) but it was probably larger, by perhaps as much as 100 times, at redshift $\sim 1 - 2$ (Ghosh and White (2001)). The star formation rate can be directly tied to the luminosity of a galaxy in several different wavelength regions, for instance the UV or X-ray bands.

SFR from XRBs

The connection between star formation rate and L_x is dominated by X-ray binaries. There are two types of XRBs: the low mass XRB (LMXB), high mass XRB (HMXB). An LMXB is a binary consisting of a neutron star or black hole and a low mass companion. The companion has filled its Roche lobe and material is falling onto the neutron star/black hole which is accreting material and radiate X-rays. The HMXBs are similar binaries, but where the star companion is a massive star with a strong stellar wind. The wind is accreting onto the neutron star/black hole. To quantify, there are about 140 X-ray objects in M31 (Andromeda galaxy) with luminosities ranging between $10^{35} - 10^{38} \text{ erg s}^{-1}$, see Kaaret (2002), that add up to a total X-ray luminosity of $\sim 3 \cdot 10^{39} \text{ erg s}^{-1}$, see Supper *et al.* (1997).

Both types of binary objects are closely tied to the SFR of the host galaxy because the more stars are created, the more stars turn into neutron stars and the more XRBs are created. In Ghosh and White (2001) (hereafter GW01) three differential equations are presented that describe

the debate continues.

the number of XRBs as a function of time and SFR. The form of the SFR used in simulations in this thesis is the peak-M (or Madau) profile which has the form:

$$\text{SFR}(z) = 2 \left(1 + \exp \frac{z}{z_{max}} \right)^{-1} (1+z)^{p+(2z_{max})^{-1}} \quad (2.7)$$

where z_{max} is the redshift where star formation peaks and p is a calibration parameter at low redshifts ($\text{SFR}(z \ll z_{max}) \propto (1+z)^p$).

The number of HMXBs follows a simple relation to SFR and time:

$$\frac{\partial n_{HMXB}(t)}{\partial t} = \alpha_h \text{SFR}(t) - \frac{n_{HMXB}(t)}{\tau_{HMXB}} \quad (2.8)$$

n_{HMXB} is the number density of HMXBs in the galaxy, τ_{HMXB} is the evolutionary timescale of the objects (here assumed to be $\sim 5 \cdot 10^6$ years, which is the approximate evolutionary lifetime of a massive star) and α_h is the rate of formation of HMXBs per unit SFR. α_h is a product of the fraction of stars in binaries, fraction of binaries with correct range of masses and fraction of binaries that survive a supernova.

LMXBs can possibly be created in two separate ways; capture of a neutron star companion to a normal star in a globular cluster where the star density is high enough, or evolution of primordial binaries. The paper, GW01, only take into account the latter since they assume that to be the dominant feature in spiral galaxies with lower space density of stars. GW01 divide the evolution of a binary to an LMXB into two stages, a post-supernova binary (PSNB) where one of the stars have turned into a neutron star, but with still no contact with the companion, and the LMXB phase where the companion has come into contact with the Roche lobe of the neutron star and transfer of material has begun. The PSNB turns into an LMXB after either nuclear evolution or orbital decay due to gravitational radiation or magnetic braking. The timescales in the PSNB/LMXB cases are τ_{PSNB} and τ_{LMXB} and are assumed, in GW01, to be ~ 2 Gyrs and ~ 1 Gyrs respectively. The equations for the number densities (n_{PSNB} and n_{LMXB}) of these objects are then defined as

$$\frac{\partial n_{PSNB}(t)}{\partial t} = \alpha_l \text{SFR}(t) - \frac{n_{PSNB}(t)}{\tau_{PSNB}} \quad (2.9)$$

$$\frac{\partial n_{LMXB}(t)}{\partial t} = \frac{n_{PSNB}(t)}{\tau_{PSNB}} - \frac{n_{LMXB}(t)}{\tau_{LMXB}} \quad (2.10)$$

In the top one of these equations, α_l is again the rate of formation of LMXBs per unit SFR.

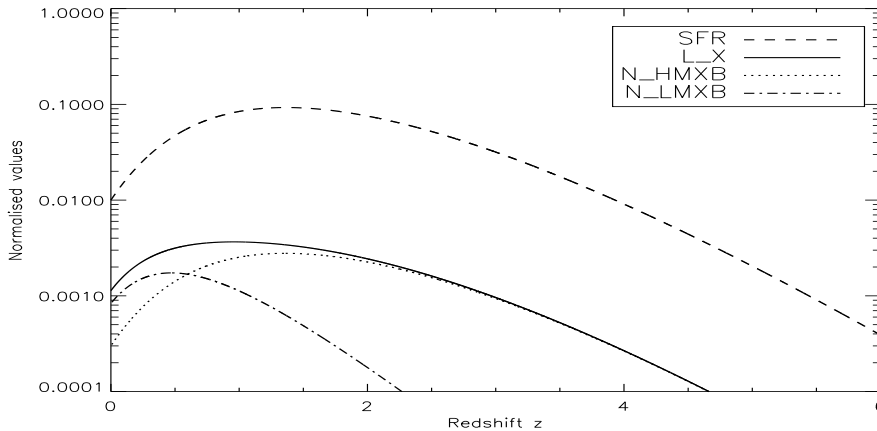


Figure 2.4: Example of result from calculation of SFR, L_x etc. This plot was made with the parameter values $p = 4.6$ and $z_{max} = 0.39$. The parameter values are chosen because they fit the Madau *et al.* (1996) sample of Lyman-break galaxies. The fits are explained in detail in Blain *et al.* (1999).

Simulations of L_x and SFR

I was given a program, based on the equations above, from Dr. Jesper Rasmussen³ in Copenhagen. The program was used to make simulations of the X-ray luminosity of disk galaxies, and is described in detail in a paper by Rasmussen *et al.* (2004). However, in order to investigate the L_x and SFR at the redshift of $z = 3.2$, I ran the program with different parameter values to see what kind of results were possible. An example of a plot can be seen in Fig. 2.4. In the plot, L_x is simply calculated as the sum of number of LMXBs and number of HMXBs, and the SFR follows the Madau profile. For the standard values of p and z_{max} of 4.6 and 0.39 respectively, the luminosity at redshift 3.2 becomes ~ 0.67 times the luminosity at zero redshift. We can draw some conclusions from the plot in Fig. 2.4. For instance, because of the differing evolutionary timescales between HMXBs and LMXBs, the fraction of HMXBs to LMXBs can reveal the time-lag since the last starburst. HMXBs will form shortly after the starburst, while the number of LMXBs will rise slowly and peak at a later time. Another factor in the population fraction is the probability of creating HMXBs/LMXBs. In the evolution of primordial binaries, the HMXBs are more probable because the companion to the dying star has a high mass and is more likely to stay in orbit when the

³jr@astro.ku.dk, Niels Bohr Institute, Copenhagen Astronomical Observatory, University of Copenhagen, Juliane Maries Vej 30, DK-2100, Copenhagen, Denmark

dying star expels its outer layers. Because of this, we expect a much larger fraction of HMXBs, but the longer lifetime of LMXBs counteracts this effect.

One important fact to remember is that the L_x in the simulations are restframe luminosities, and because we assume a power law, that luminosity can be drastically more than the one we actually observe in a typical interval of 0.3 - 8 keV. Let us assume we *observe* in an energy interval X_1 to X_2 . Redshifting of a wavelength is linearly proportional to $(z + 1)$ towards longer wavelengths, which will translate to an inverse relation in energy, because energy and wavelength are inversely dependent. This means that the energy interval in the restframe is $(z + 1)X_1$ to $(z + 1)X_2$. Now, the luminosity is the integral over a normalization factor times the power law, giving:

$$\frac{F_{obs}}{F_{em}} = \frac{\int_{X_1}^{X_2} N \cdot E^{-\Gamma} dE}{\int_{(z+1)X_1}^{(z+1)X_2} N \cdot E^{-\Gamma} dE} = \dots = (z + 1)^{\Gamma-1} \quad (2.11)$$

For the case of redshift $z = 3.2$, some relations between observed and emitted fluxes for different photon indices, Γ , can be seen in Table 2.3.3.

Table 2.3.3	
Ratio of observed to emitted X-ray flux	
Photon index	$\frac{F_{obs}}{F_{em}}$
1	1.00
1.5	2.05
2.0	4.20

Including this effect, the observed flux of a source at redshift 3.2, with the standard values mentioned before, becomes $\sim 1.38 F(z=0)$ for photon index 1.5.

In the program described above, the X-ray luminosity comes indirectly from the SFR, assumed to follow some function (for instance Madau). But if we instead have an observational value of the X-ray luminosity, the SFR can be calculated from it. Ranalli *et al.* (2003), find empirical relations between SFR and soft/hard X-ray luminosity:

$$\text{SFR} = 2.2 \cdot 10^{-40} L_{0.5-2\text{keV}} M_{\odot}/\text{yr} \quad (2.12)$$

$$\text{SFR} = 2.0 \cdot 10^{-40} L_{2-10\text{keV}} M_{\odot}/\text{yr} \quad (2.13)$$

One is interested in constraining the SFR because we want to know which function the SFR follows best, thereby telling us for instance when star formation peaked, or when star formation started.

Connection star formation - AGN?

Is there a connection between star formation and AGN activity? Fernandes *et al.* (2001) study circumnuclear starbursts in Seyfert 2 nuclei and find that the bursts are powerful, surrounding powerful AGNs. They also find an apparent luminosity link between the starburst-AGN luminosity, and interpret this as fuelling of the AGN central black hole by stirred up gas from the starburst activity. Another possibility, suggested by Chokshi (1997), is that jets coming out from an AGN can induce star formation by producing over-pressured cocoons.

2.3.4 Classifying an X-ray source

How do we tell the difference between observing an AGN or a collection of XRBs? The first and major difference is of course the luminosity. The luminosity of an AGN ranges, as seen in section 2.3.2, from 10^{40} erg s $^{-1}$ and upwards, while the typical luminosity of an XRB is $< 10^{38}$ erg s $^{-1}$ (the Eddington luminosity of a neutron star). Typically we assume that there will be no more than ~ 150 XRBs in a galaxy, based on studies of nearby star-bursting galaxies, for instance the study of the merging Antennae galaxy by Fabbiano *et. al* (2004). Therefore, a galaxy with an $L_x \gtrsim 10^{40}$ erg s $^{-1}$ will almost certainly be an AGN. It is only when we go to lower luminosities that we will have to find other characteristics separating XRBs from AGN.

All of the mentioned methods for creation of X-rays, in section 2.3.1, require highly excited electrons and/or very hot gas. The source of highly excited electrons is often a hot gas, and hot gas can be found in several surroundings. One example is the corona of a star, which is a very hot and thin gas. Another example could be the inner regions of an accretion disk surrounding an XRB. The blackbody spectrum of the accretion disk is a characteristic that separates a collection of XRBs from AGNs. We have seen, in section 2.3.2 about AGNs, that the change in energy, which is basically the same as luminosity is

$$\dot{E} \propto L \propto \frac{GM}{R} \cdot \dot{M} \quad (2.14)$$

According to the Stefan-Boltzmann law, we also have that

$$L \propto R^2 T^4 \quad (2.15)$$

Combining eq. 2.14 and eq. 2.15, neglecting all constants, we get:

$$T^4 \propto \frac{M}{R^3} \dot{M} \quad (2.16)$$

With the proper constants and typical values for an XRB, the peak temperature of the accretion disk will lie in X-rays. Comparing with this, we

see that because the mass of the central black hole in an AGN is larger but the radius of the accretion disk is also larger, the peak of the continuum will be at lower temperature/longer wavelength, e.g. the big blue bump. Because of this, the peak of the continuum is a distinguishing property. The source of X-rays in an AGN are instead non-thermal processes, such as bremsstrahlung, synchrotron radiation and inverse Compton radiation.

Another thing that can be used to separate an AGN from a collection of XRBs is the variability of the source. The variability of any source cannot be shorter than the time it takes the information about the change to cross the surface of the object. Hence, the size limits the variability by $\delta t > \frac{R}{c}$. From this we understand that variability in an XRB can have timescales much shorter than an AGN. However, we expect the variability of an AGN to be greater in amplitude and with shorter periods than from a collection of XRBs because the several small, varying sources will cancel each other out.

The next thing to test is the hardness ratio. When calculating a hardness ratio, one divides the number of counts from the source in one energy interval with the number of counts in another energy interval, for instance 0.5 - 2 keV and 2 - 8 keV. If the ratio of counts between the soft and hard bands is low, the source is classified as hard, and conversely soft if the ratio is high. Hard sources usually imply that the softer part of the X-ray spectrum has been absorbed along the way, in turn implying that we are watching the source through for instance a torus, as in the unifying theory for AGNs. This in turn would classify the AGN as a type 2 AGN/Seyfert. The hardness ratio can also be used to separate galaxies from AGNs. In Norman *et al.* (2004), they want to find the luminosity function of normal galaxies in the Chandra Deep Fields North and South and their sample consists of almost 450 galaxies. When they plot the hardness ratio of each source against the soft X-ray luminosity they find that type 2 AGN/Seyferts have harder spectra with a large span in luminosity. Both type 1 AGN/Seyferts and galaxies have correspondingly softer spectras but they differ in luminosity, with AGNs being much brighter than galaxies. Hence the conclusion is that a combination of hardness ratio and luminosity should be able to separate normal galaxies from AGNs.

2.4 Infrared theory

The sources studied in this thesis are located so far from us that the restframe wavelength of observed near-IR corresponds to visual or blue. The luminosity at these wavelengths comes from long-lived A and F stars and will hence give a measure of the stellar mass of the galaxies. But observations in infrared are also interesting for galaxies at other redshifts,

because the origin of infrared light can also be reprocessing of more energetic light in dust clouds surrounding a bright source. A strong correlation between radio emission and far-infrared emission has been found in infrared luminous galaxies (Condon (1992)). This could be indicative of star formation, if we assume that the far-infrared luminosity comes from reprocessing of light from young stars, still embedded in their nursery nebula, and the radio luminosity comes from synchrotron radiation in recent supernovas (Smail (2002)). After the first satellite (COBE) had studied the cosmic microwave background, a second component to the background was discovered that peaked at $\sim 100 - 200 \mu\text{m}$. Smail (2002) explains how this far-infrared background can originate from a large population of star forming galaxies at high redshift. He even concludes that a majority of all stars in the Universe could have been created in these galaxies.

Chapter 3

Sample, method and results

3.1 Ly α sample

15 sources with bright Ly- α emission were investigated. Coordinates for the sources, labeled 1 to 15, are found in Table 3.1.1. The 15 sources were found by my supervisor Johan Fynbo, by measuring the intensity of the source in the OIII/3000+51 filter, hereafter named the N filter, (central wavelength 5105 Å) of FORS1/VLT. This filter corresponds, approximately, to the rest wavelength of Ly α at redshift 3.2. The intensity in the N filter, compared to the intensity in two other filters (a summed filter of B99 and V89 at WFI/La Silla with central wavelengths 4562.52/5395.62 Å and Rc162 at WFI/La Silla with central wavelength 6517.25 Å), decides the redshift of the source as described by Fynbo *et al.* (2003). The sensitivity curves of the four filters can be seen in Fig. 3.1. The magnitudes in the narrow filter can be found in Table 3.1.2.

3.1.1 Coordinate transformation

At the start of this project, the only known positional coordinates of the sources were the pixel coordinates on the CCD. Hence, the first task to be completed was a calibration to R.A. and Dec. Two methods were attempted. A world calibration of the image, and a manual transformation by means of measuring the pixel coordinates of several stars in the image and comparing them to already calibrated images from the ESO Imaging Survey¹. After assuming a non-rotated translation, the resulting manual transformation became:

$$\begin{pmatrix} \text{R.A.} \\ \text{Dec} \end{pmatrix} = \begin{pmatrix} 169359.69'' \\ -100154.34'' \end{pmatrix} - 0.20041'' \cdot \begin{pmatrix} x \\ y \end{pmatrix} \quad (3.1)$$

Reversed calculations of R.A./Dec to x/y of a number of other stars gave an error estimate of less than 1''. The world calibration turned out to

¹www.eso.org/science/eis

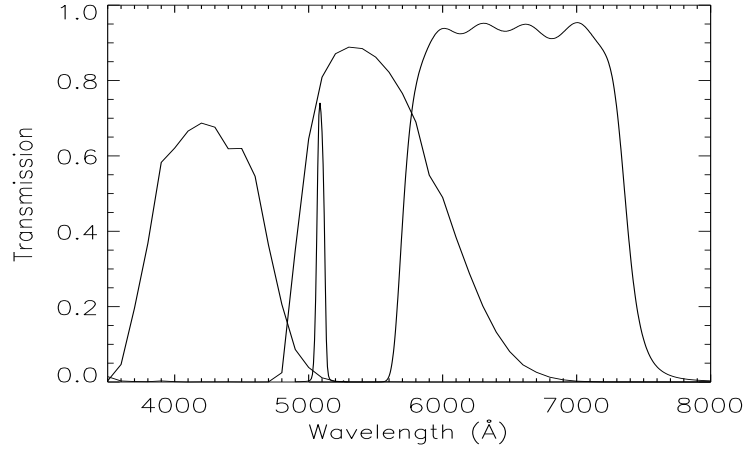


Figure 3.1: Response curves of the Ly α selection filters.

have the same, or larger, errors and the manual calibration was employed. Using this transformation, the coordinates of the 15 Ly α -sources can be found in Table 3.1.1.

Table 3.1.1		
Coordinates of Ly α -sources		
Source	R.A	Dec
1	3 : 32 : 14.82	-27 : 44 : 18.3
2	3 : 32 : 15.78	-27 : 44 : 11.0
3	3 : 32 : 30.85	-27 : 47 : 53.7
4	3 : 32 : 30.82	-27 : 47 : 19.9
5	3 : 32 : 31.48	-27 : 43 : 37.6
6	3 : 32 : 13.42	-27 : 47 : 44.9
7	3 : 32 : 14.57	-27 : 45 : 53.4
8	3 : 32 : 12.46	-27 : 42 : 46.4
9	3 : 32 : 14.58	-27 : 43 : 26.8
10	3 : 32 : 17.59	-27 : 43 : 42.9
11	3 : 32 : 29.51	-27 : 43 : 57.8
12	3 : 32 : 31.59	-27 : 46 : 27.6
13	3 : 32 : 30.04	-27 : 48 : 38.0
14	3 : 32 : 11.46	-27 : 48 : 21.0
15	3 : 32 : 31.52	-27 : 47 : 35.6

3.1.2 Luminosity of Ly α -sources

The measurements of the fluxes in Ly α was made in MIDAS, using a program written by supervisor Johan Fynbo. The program measures the

number of counts in a circle with a certain pixel radius centred on any object chosen. Then the same aperture is placed on 15 random positions close to the original source. These random positions are chosen so as to not lie on top of any other bright object. After the random measurements, the program displays number of counts with background subtracted, and the error in counts.

For the Ly α luminosity measurements, in the narrow band, the aperture diameter was chosen to 15 pixels. The conversion from counts to flux/luminosity was also given to me by my supervisor Johan Fynbo. The conversion to magnitude reads:

$$M_{AB} = 34.33 - 2.5 \cdot \log_{10}(\text{counts}(\text{in aperture with 30 pix. diameter})) \quad (3.2)$$

which translates to flux by:

$$F_{Ly\alpha} = \frac{10^{-0.4(M_{AB}+48.60)} \cdot 3 \cdot 10^{18} \cdot w}{cw^2} \text{ erg s}^{-1} \text{ cm}^{-2} \quad (3.3)$$

where cw is the central wavelength of the filter in Angstroms (5105.00 Å) and w is the width of the filter, also in Angstroms (60 Å). In order to get number of counts in an aperture with 30 pixel diameter from the same in a 15 pixel diameter aperture, the counts from a bright star was measured with both apertures and a conversion calculated. The reason to not get the counts in a 30 pixel diameter aperture from the beginning is that the S/N (signal-to-noise ratio) of the sources increased with decreased pixel diameter. The luminosity of the sources in the narrow filter can be found in Table 3.1.2. Errors are the ones given by the program. The Star Formation Rate, derived by Kennicutt (1983) for L(H α), with L(H α) = L(Ly α)/8.7 derived by Brocklehurst (1971), used here reads:

$$\text{SFR} = \frac{L(\text{Ly}\alpha)}{8.7 \cdot 1.12 \cdot 10^{41}} M_{\odot}/\text{yr} \quad (3.4)$$

where the luminosity is given in erg s⁻¹. These SFR are lower estimates to the real value, because of dust obscuration, see e.g. Charlot & Fall (1993).

3.2 X-ray sample

3.2.1 CXO, Chandra Deep Field South and GOODS

The Chandra X-ray Observatory, CXO, has a better resolution than other current X-ray telescopes, but observes a smaller area of the sky. It was launched in 1999 and is run by NASA. It consists of a tube with four pairs of paraboloid and hyperboloid mirrors, focusing the X-rays onto the science instruments. CXO has two cameras in the focal plane, ACIS and

Source	Magnitude in N	Ly α luminosity (erg s $^{-1}$)	SFR (M $_{\odot}$ /yr)
1	24.31 \pm 0.05	(4.96 \pm 0.23) \cdot 10 42	5.09 \pm 0.24
2	25.07 \pm 0.06	(2.46 \pm 0.14) \cdot 10 42	2.53 \pm 0.14
3	23.98 \pm 0.05	(6.69 \pm 0.32) \cdot 10 42	6.86 \pm 0.33
4	25.33 \pm 0.22	(1.93 \pm 0.44) \cdot 10 42	1.98 \pm 0.45
5	24.25 \pm 0.03	(5.25 \pm 0.15) \cdot 10 42	5.39 \pm 0.15
6	25.64 \pm 0.26	(1.46 \pm 0.39) \cdot 10 42	1.50 \pm 0.40
7	25.63 \pm 0.16	(1.47 \pm 0.23) \cdot 10 42	1.51 \pm 0.24
8	25.09 \pm 0.11	(2.41 \pm 0.26) \cdot 10 42	2.47 \pm 0.27
9 ^a	24.87 \pm 0.31	(2.96 \pm 0.98) \cdot 10 42	3.03 \pm 1.01
10	25.44 \pm 0.26	(1.75 \pm 0.47) \cdot 10 42	1.80 \pm 0.48
11	24.85 \pm 0.13	(3.01 \pm 0.38) \cdot 10 42	3.09 \pm 0.40
12	24.36 \pm 0.05	(4.75 \pm 0.22) \cdot 10 42	4.88 \pm 0.23
13	25.42 \pm 0.03	(1.79 \pm 0.05) \cdot 10 42	1.84 \pm 0.05
14	25.61 \pm 0.41	(1.50 \pm 0.69) \cdot 10 42	1.54 \pm 0.71
15	25.84 \pm 0.30	(1.21 \pm 0.39) \cdot 10 42	1.24 \pm 0.40

^aThis is the blob which is very extended. That could be the reason for the larger error.

HRC, and two spectrometers that can be turned into or out of the focal plane. With the ACIS-camera (Advanced CCD Imaging spectrometer) the sensitivity is in the range 0.3 - 8 keV. The sensitivity is plotted in Fig 3.2. The pixel size varies in the different images used, but is $\geq 0.5''$.

The 15 Ly α -sources overlap the Chandra Deep Field South (CDFS). The CDFS is one of the two fields targeted in the GOODS (the Great Observatories Origins Deep Survey²) program. The program is an international joint project between space-based and ground-based telescopes. The aim is to get new results on galaxy formation, stellar evolution and to study active galactic nuclei over a large range of redshift. Two patches of sky, one in the northern sky (Hubble Deep Field North) and one in the southern sky (CDFS), are therefore studied in great depth by a large number of instruments, mainly the HST, CXO and VLT. The CDFS is a 12'x12' field centred on R.A = 3^h32^m28.286^s and Dec. = -27°56'34.10". The full exposure is a composite of eleven exposures with a combined exposure time of just above 99000 seconds. The images used in this thesis from CXO can be downloaded freely from the homepage of *Chandra*³.

²www.stsci.edu/science/goods

³<http://chandra.harvard.edu/>

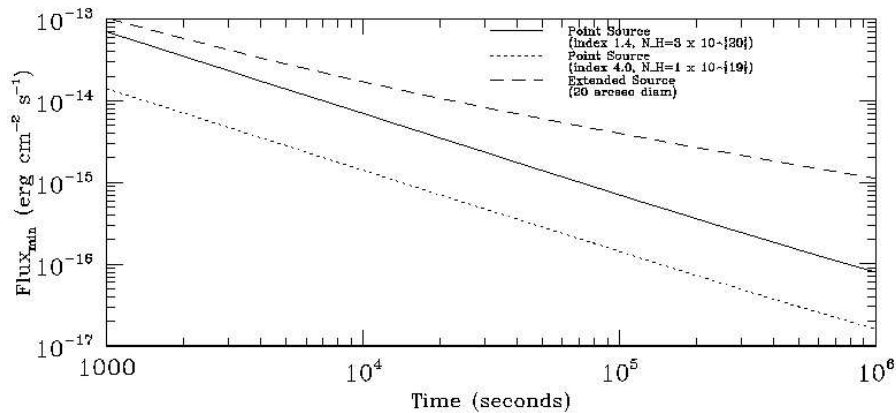


Figure 3.2: Sensitivity of ACIS-camera on CXO. From *Chandra* homepage, credit of NASA/CXC/SAO.

3.2.2 Measurements and results

First attempts

At first the locations of the 15 sources were investigated visually in the *Chandra* image with no detections. A list of sources constructed by wavelet-technique (using WAVDETECT, see Freeman *et al.* (2002)) was provided and I attempted to correlate sources from that list to the coordinates of the sources listed in Table 3.1.1. This yielded a few candidates, but often a bit too far away from the actual source (i.e. $\Delta R.A./\Delta Dec > 1''$) and with too low signal-to-noise (i.e. $S/N < 2$) to be promising. Next, small rectangles surrounding each of the sources was cut out and the images stacked on top of each other, also with a discouraging result of no detection.

All measurements of magnitudes or fluxes/luminosities were carried out in the same fashion. Circles of a certain pixel radius were placed over the position of the source and the number of counts in that circle were found. A second circle, with greater circle radius was also centred on the source position and the number of counts calculated. Finally, a third circle with even greater radius was centred and number of counts measured. The number of counts in the middle circle were subtracted from the number in the outermost circle. This gave the background counts. Finally these counts were subtracted, scaled by area, from the innermost circle counts. The resulting counts were assumed from the source. The radii of the circles were determined from exposure to exposure by extracting the source counts from any chosen source in the neighborhood

of the Ly α -sources in circles with different radii. The source counts were plotted as a function of the radius of the inner circle radius. At first the curve increases, but at a certain radius the curve stays constant, or even starts declining. This is the radius chosen for the inner circle. Usually the other circle radii are 4/8 pixels larger.

In order to get an unbiased result, the number of counts from each source was measured within a circle of certain radius. During the calibration of these circles we realized that the image was altered in two ways, which made it impossible to use. First, it was a stacked image of eleven exposures which, if the positions were not well correlated, would smudge any faint image. Secondly, in order to facilitate visual examination, four pixels were smudged to one (making the pixels 4''x4''), also reducing the visibility of any faint, point-like source. New images of each unsmudged exposure were retrieved.

Second attempts

The new images had a pixel size of 2''. I was given an IDL-program, written by thesis supervisor Kristian Pedersen, that calculates number of counts within circles of differing radius, according to the description above. To calibrate the radii of the circles, calculations were made on a bright, point-like source near the area where the Ly α sources are found, with differing circle radii. The source counts stabilised for a centre radius of four pixels, and after careful examination the other circle radii were determined to eight and twelve pixels respectively. Two of the sources (Source # 8 and # 11) were located very close to bright sources (but far enough not to be detections of the Ly α galaxies). In order to measure the background of these sources, without biasing it by the bright source, the outer circle was displaced compared to the centre so that it was not biased by either actual or false source. The second measurements were made in the individual exposures (in total eleven) and the results added.

To convert number of counts to flux the program XSPEC, also found at the *Chandra* homepage, was used to calculate the sensitivity of the detector. This was calculated for an area 4' from the centre of the image, with $N_H = 0.1 \cdot 10^{22}$ atoms/cm² and photon index 1.5. N_H is the amount of absorbing hydrogen in our own galaxy and is dependent on how far from the galactic plane we observe. The number used here was calculated with the Colden⁴: Galactic Neutral Hydrogen Density Calculator. The photon index is the slope of the spectrum from the source. The choice of photon index was based on extensive studying of papers concerning the CDFS. A photon index of 1.5 seem favourable in this area, see for instance the work of Giacconi *et al.* (2001). The luminosity was then

⁴<http://cxc.harvard.edu/toolkit/colden.jsp>

calculated using the luminosity distance at $z = 3.2$. Some of the sources (# 3, # 13 and # 15) were situated on the dark cross between the CCD-cameras in all exposures, and their fluxes could not be determined. The second results are not included here because of the poor quality of the results.

Last attempts: Final results

After the second results, I attempted at finding the hardness ratio, to try to determine if the sources were type 1 or type 2 AGN. The hardness ratio was determined by dividing the image into energy bands between 0.5 - 1 keV, 1 - 2 keV, 2 - 4 keV and 4 - 8 keV, and counting the number of counts in the same way as for flux determinations. Because of the low number of counts, making it impossible to get a valid result when dividing them into different energy bands, the image was resolved again into a finer resolution, this time to pixel size $0.5''$. However, this triggered a third attempt at finding the fluxes of the sources. This time, the circle radii for flux determinations were determined to 6, 9 and 13 pixels respectively. The new results, found in Table 3.2.2, yielded more positive sources, but with lower S/N. The errors in the table are purely statistical, and there are systematic errors of $\sim 25\%$ on all fluxes/luminosities. Sources # 3, # 13 and # 15 were situated on the dark cross between the CCD-cameras and were therefore not measurable.

Source	Counts	L_x ($\text{erg} \cdot \text{s}^{-1}$)
1	2.73 ± 7.01	$(3.12 \pm 8.00) \cdot 10^{42}$
2	3.32 ± 6.95	$(3.81 \pm 7.92) \cdot 10^{42}$
3	---	---
4	3.73 ± 6.36	$(4.27 \pm 7.25) \cdot 10^{42}$
5	-1.00 ± 6.14	---
6	12.86 ± 8.36	$(1.48 \pm 9.59) \cdot 10^{43}$
7	-3.95 ± 8.18	---
8	11.32 ± 8.56	$(1.30 \pm 9.83) \cdot 10^{43}$
9	3.64 ± 6.49	$(4.17 \pm 7.45) \cdot 10^{42}$
10	6.50 ± 7.43	$(7.43 \pm 8.54) \cdot 10^{42}$
11	-10.14 ± 6.16	---
12	3.05 ± 7.63	$(3.49 \pm 8.72) \cdot 10^{42}$
13	---	---
14	5.18 ± 7.20	$(5.93 \pm 8.23) \cdot 10^{42}$
15	---	---

The sources that have the greatest S/N (in the final measurements) were stacked (source # 6, # 8, # 10 and # 14) and a hardness ratio found

for the combined image. Dividing the number of counts in the band 0.5 - 2 keV with the same in 2 - 8 keV revealed a possible hardness ratio of 0.42 ± 0.66 . This could be compared to the results of a paper by Gandhi *et al.* (2004), as discussed in chapter 4. A stacking of all (twelve) sources was made by cutting out thumb-nail images centred on each source and stacking them on top of each other. There was still no detection, setting an upper limit to the average luminosity of each source of $8.74 \cdot 10^{42}$ erg s⁻¹, for a detection with S/N > 2. The effective exposure time in the stacked image is 11.9 Ms. This limiting luminosity corresponds to $\sim 1850 M_{\odot}/\text{yr}$, from the Ranalli *et al.* (2003) estimates, which is much too large to be realistic.

3.2.3 Error calculation and randomness

Errors in the results come from several error sources. The statistical errors come from assuming a Poisson distribution in the number of counts. The counting error due to this was calculated using the formula:

$$\text{S/N} = \frac{\text{source}}{\text{err.source}} = \frac{n_a - k \cdot (n_c - n_b)}{\sqrt{n_a + k^2 \cdot (n_c + n_b)}} \quad (3.5)$$

where n_a , n_b and n_c are the number of counts in the inner, middle and outer measuring circles respectively and k is the area conversion factor between the outer ring and the inner circle.

There are also several systematic errors such that different simulations with XSPEC, done with the same parameters, yielded different results in sensitivity. Therefore, ten runs were made and a systematic contribution to the error calculated. There are two parameters that are chosen in XSPEC, the distance from the optical axis and photon index. We chose $4'$ and $\Gamma = 1.5$ since our sources mostly stay within that area, and since that photon index seem to be favourable in the *Chandra* deep field images. However, to investigate the effect of an error in these parameters, we calculate the flux for sensitivity area $2'$ and $6'$ and for $\Gamma = 1.0$ and $\Gamma = 2.0$ and take the relative error. Of all these error sources, photon index is the greatest, and the combined systematic error seems to be ~ 25 % in all measurements, independent of flux.

I also calculated the number of random galaxies that would appear in my centre circle at that luminosity. According to the log N - log S diagram in Rosati *et al.* (2002) there are about 11000 objects $\cdot \text{deg}^{-2}$ that shine with $L_x \geq 8 \cdot 10^{-17}$ erg cm⁻² s⁻¹ which was the flux limit of the stacked image. This, combined with my centre circle of radius about $6''$, gives that there should be 0.09 objects shining more brightly than the flux limit in each measured ring. The chance of accidentally seeing another galaxy is approximately one in eleven. To further investigate the possibility of random effects, circles of the same radii were placed at

26 random positions in the image, where nothing was seen with the eye. Of the 26, ten were positive and 16 negative. The S/N of the random sources was consistent with a normal distribution, i.e. about 30 % of them had $S/N \gtrsim 1$ or $\lesssim -1$. This means that the error estimates are correct. Studying the results of Table 3.2.2 we see that approximately a third of the sources has $S/N \sim \pm 1$ (three or four out of twelve) which therefore is consistent with just random noise.

3.3 Infrared and optical sample

Next, the idea was to study the sources in infrared, as these wavelengths in the rest frame corresponds to visual/blue light where A and F stars shine their brightest. Because these stars have a longer lifetime than the most massive stars, they will be a measure of the number of stars in the galaxy. Also, infrared images from ISAAC in the GOODS field are rather deep and readily available. The luminosity in the broad-band images studied here are a result of the work of another MSc student, Brian Krog.

3.3.1 ISAAC

ISAAC (Infrared Spectrometer And Array Camera) is an instrument at the UT1-telescope at Paranal, VLT, Chile. It is capable of low and medium resolution spectroscopy and imaging between 1 - 5 μm . The observations were taken as a part of the GOODS project in the J, H and K bands with central wavelength 1.25 μm , 1.65 μm and 2.16 μm respectively and exposure times ranging from 2 - 7.5 hours. The width of the filters is approximately 0.3 μm for all. The goal for the different bands in the GOODS survey is to reach a magnitude of approximately 25, but not all fields are completed yet. The pixel size of the images is 0.15".

3.3.2 ISAAC measurements and results

The counts of the sources are measured in the same way as for the X-ray images (described in detail in section 3.2.2) by measuring number of counts within three circles centred on the source. The circle radii for flux measurements were determined to be 7, 15 and 20 pixels respectively. Two of the sources, # 8 and # 9, were not covered by the ISAAC-fields and source # 13 was completely impossible to study due to extreme saturation of a foreground star. Of the rest, none were detected. The sources, after subtraction of the background, were all well below any kind of flux detection limit. I calculated the magnitude necessary for a $S/N \geq 2$ detection and the magnitude limit lies between 23.5 and 24

in the individual images of the J, H and K bands. The only possible conclusion here is that our sources are not brighter than this.

3.3.3 Visual broad band measurements

For comparison, I include the results from a MSc-student at Århus University, Brian Krog⁵, based on HST observations with the Advanced Camera for Surveys (ACS). He has obtained the magnitudes in the B, V, I and Z bands for the same 15 sources as are studied here. The details of the filters, with exposure times are found in Table 3.3.4. Four of the

Band	Filter name	λ_c (Å)	$\delta\lambda$ (Å)	Exp. time (s)
B	F435W	4297	1038	17100
V	F606W	5907	2342	14250
I	F775W	7764	1528	14250
Z	F850LP	9445	1229	28500

sources had double components, Source # 2, # 8, # 11 and # 13. The components have here been added into one, since the separation is impossible to see in the less resolved images of *Chandra*. The separation should be possible to see in the ISAAC images, but since we have no detections whatsoever in the infrared, it is of no relevance to include the two components. The results are found in Table 3.3.5. We expect the magnitudes in B and V bands to be larger than the same in Ly α (N filter) because that is a selection bias, we choose candidates with large flux discrepancy between the narrow Ly α centred band and near broad bands. The central wavelength of B and V filters in Table 3.3.4 corresponds nearly to the broad band filters used in the selection of the sources, see section 3.1. We also expect only minor differences between the different broad bands, since we are measuring the continuum of the sources.

3.4 Radio counterparts

A large portion of AGNs have radio counterparts, see section 2.3.2. Attempts were made to find such counterparts, since they would confirm the presence of an AGN. Only AGNs can create the necessary conditions for observing radio counterparts at that distance. Several databases, such as NED, SIMBAD, the VLA Archive and the CENCOS database⁶

⁵briank@phys.au.dk, Institut for Fysik og Astronomi, Århus Universitet, Ny Munkegade Bygn 520, 8000 Århus C.

⁶<http://cencosw.oamp.fr>

Table 3.3.5				
Magnitudes from Brian Krog				
Source	Magnitude in V	B - V	V - I	V - Z
1	27.19 ± 0.08	0.94 ± 0.14	-0.04 ± 0.12	-0.11 ± 0.15
2	25.04 ± 0.05	1.00 ± 0.11	0.21 ± 0.09	0.14 ± 0.11
3	27.31 ± 0.07	1.71 ± 0.21	-0.77 ± 0.17	-0.87 ± 0.23
4	27.65 ± 0.11	0.61 ± 0.18	0.15 ± 0.17	-0.35 ± 0.26
5	27.10 ± 0.08	0.94 ± 0.13	-0.46 ± 0.14	-0.72 ± 0.21
6	27.51 ± 0.11	1.40 ± 0.29	0.28 ± 0.16	-0.40 ± 0.27
7	27.34 ± 0.08	0.40 ± 0.11	-0.20 ± 0.12	-0.58 ± 0.19
8	25.76 ± 0.05	1.39 ± 0.20	0.20 ± 0.11	-0.52 ± 0.20
9	28.12 ± 0.14	0.56 ± 0.25	0.79 ± 0.16	0.59 ± 0.22
10	27.32 ± 0.09	0.61 ± 0.14	-0.20 ± 0.15	-0.73 ± 0.26
11	26.75 ± 0.08	0.25 ± 0.13	0.13 ± 0.13	-0.03 ± 0.16
12	26.42 ± 0.07	0.95 ± 0.10	0.31 ± 0.08	0.10 ± 0.10
13	27.73 ± 0.15	---	---	---
14	26.57 ± 0.06	-0.09 ± 0.10	0.29 ± 0.10	0.48 ± 0.11
15	26.47 ± 0.07	2.24 ± 0.23	0.42 ± 0.08	0.36 ± 0.09

were searched. Only one of the sources had a radio source nearby. Close to Source # 11, NED found NVSS J033229-274356 at coordinates R.A./Dec.: = $3^h32^m29.4^s$ and = $-27^\circ43'56''$. This differs in position $\sim 1.5''$ in both coordinates from the Ly α source. However, the radio source was fairly weak (flux density S = 5.6 mJy) and the error in coordinates can apparently then be large, as large as $7''$ (see Condon *et al.* (1998)). Hence, the radio source may or may not be associated with the Ly α source.

Chapter 4

Discussion

I have studied a sample of 15 galaxies at redshift 3.2 in several wavelength regimes, in order to draw conclusions about the star formation rate at that redshift. I also wanted to find the contamination of AGNs in the sample. I will here discuss the results of each wavelength interval and draw some conclusions in the end about the total result of this work.

Ly α and broad-band results

It was not an objective of this thesis, to measure the Ly α flux, or the flux in other visual filters. However, the observations in Ly α were given to me, to compare with other results and the measurements were fast. Also, the values in the optical filters had already been determined by master student Brian Krog, and are of interest in understanding the nature of these objects. As we see in tables 3.1.2 and 3.3.5, the fifteen objects are fairly strong in Ly α and fairly weak in the visual bands. This is of course a selection bias, because we choose objects that have a large difference in colour between the narrow and broad bands. But it is an effective way of finding these optically faint galaxies. The star formation rates calculated from the Ly α luminosities are low, but not unreasonably low, and set a lower limit to the actual SFR, due to dust obscuration.

X-ray results

Much effort was put into careful examination of the flux of the 15 sources in X-rays. The first attempts, of visual confirmation and using the wavelet technique, failed but with the finer resolution of the second images used, a result was obtained. These results turned out to be of poor quality, because of smudging, and the last results, in Table 3.2.2, are the ones to be studied. The errors in the table are only the statistical errors. As noted in section 3.2.3, there are systematic errors of about 25 % on all values. The largest S/N is 1.54 for source # 6, without systematic errors,

and we conclude that the detections of the sources are not statistically significant. The limit after stacking the images to the summed exposure time of 11.9 Ms was, for the average source, $\sim 8 \cdot 10^{-17}$ erg cm $^{-2}$ s $^{-1}$ which equals a luminosity, at redshift 3.2, of $\sim 9 \cdot 10^{42}$ erg s $^{-1}$. Since this is just an upper limit, which if it came from only XRBs would imply between 1000 - 100000 of them, we cannot draw any conclusions of the SFR from the theory of SFR from XRBs, see section 2.3.3. The upper limit set to the SFR by this luminosity, from the equations of Ranalli *et al.* (2003), is ~ 1900 M $_{\odot}$ /yr which is an unlikely value. This limiting luminosity would also imply a lower limit to a potential black hole in the centre of about $7 \cdot 10^4$ M $_{\odot}$ according to the Eddington limit, see Eq. 2.6. Of course this limit could be lower if the luminosity of the source is less.

There is a problem in that we do not know exactly the contribution of AGNs to the sample. In a paper by Reddy and Steidel (2004), concerning the same questions as this thesis, namely the star formation in high redshift galaxies but in the GOODS Field North, they try to eliminate the AGN contribution by searching for radio counterparts, or studying the UV spectrum of the source for AGN-like emission lines. The search for radio counterparts was performed with these sources, with the conclusion that all but one do not have counterparts, with the possibility that the one that did have a radio counterpart was actually not connected to the Ly α source. That would indicate that we are not seeing AGNs, and if they are AGNs that they are very weak.

Reddy and Steidel (2004) estimate a SFR in galaxies with $2.5 < z < 3.0$ of ~ 70 M $_{\odot}$ /yr from the X-ray luminosity, using the Ranalli *et al.* (2003) estimates. That is a more reasonable SFR. Their sample consists of > 100 spectroscopically confirmed high redshift galaxies, which they stack in order to get the best possible sensitivity. A stacking was also attempted with the sources in this thesis, although the sample is much smaller. This gave the lowest limiting average luminosity of the sources.

To check whether the choice of circle sizes in the measurement proceedings was the best choice possible, the strongest sources (# 6, # 8, # 10 and # 14) were recalculated for differing circle sizes. The result was that in all but one case, the initial circle sizes gave the largest S/N. This made us confident that the method of determining circle sizes from point-like sources was correct in all measurements. Plots of the alleged position of the X-ray sources, with the Ly α source contours over-plotted were created. For the three strongest sources, the result is seen in Fig. 4.1. We see that the Ly α emission is fairly extended. We can conclude that the final measurements used better circle sizes, especially the inner circle completely matched the average extension of the Ly α sources.

The hardness ratio found by stacking the four sources with greatest S/N (see section 3.2.2) of 0.42 ± 0.66 implies a hard source, with much

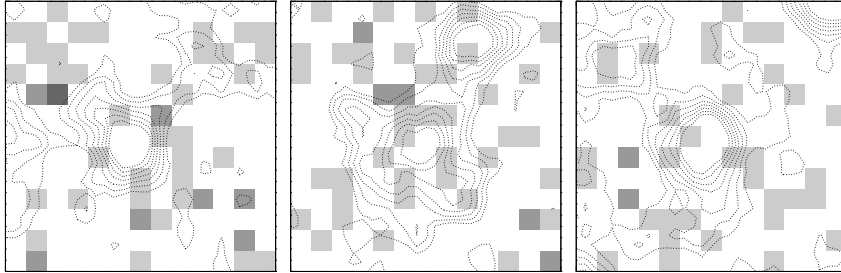


Figure 4.1: Cut-out of source # 6, # 8 and # 10 from the CXO image with contours of the Ly α emission overlaid. The images are 6'' across.

dust obscuration. In the paper of Gandhi *et al.* (2004) they categorise sources with hardness ratio < 2.5 as hard and < 1.5 as “very hard”. They also find that of their sample, observed with *Chandra*, some 20 - 50 % are classified as hard. They primarily study the use of hardness ratios, in combination with optical detections, as tools in finding Type 2 quasars but they also find that hard sources are generally less bright than soft ones and that the X-ray to K-band flux can be indicative of powerful accretion activity. Gandhi *et al.* (2004) also argue that the hardness ratio in X-rays may not necessarily correlate to reddening, but may indeed be indicative of unusual dust to gas ratios or in fact starburst activity. The hardness ratio of the sources studied here should however not be taken with great seriousness, because of the realistic risk that the so-called sources are just random noise.

We are interested in knowing how many AGNs we should see in our volume, down to the sensitivity limit that we have. For this, we use the luminosity function Φ , describing number of AGNs per volume. In a paper by Miyaji *et al.* (2000), using data from the ROSAT¹ satellite, we find such a luminosity function (Fig. 3a and b in that paper) for different redshifts and cosmological parameters and for the 0.5 - 2 keV band. In this calculation we choose an $H_0 = 75 \text{ km s}^{-1} \text{ Mpc}^{-1}$, $\Omega_M = 0.3$ and $\Omega_\Lambda = 0.0$ universe. Our limiting luminosity in that band is $\sim 1.5 \cdot 10^{43} \text{ erg s}^{-1}$ for a S/N = 2 detection. This is unfortunately lower than the least luminous point calculated for the redshift bin 2.3 - 4.6, in Miyaji *et al.* (2000). To get an upper estimate on number of AGNs however, we extrapolate the seemingly linear relation followed at greater luminosities. The resulting Φ becomes $7.03 \cdot 10^{-5} \text{ Mpc}^{-3}$. We also have to calculate the comoving volume that we observe, using the area of the sky we observe and the “redshift width” of the narrow Ly α filter. This was done using a program given to me by supervisor Johan Fynbo, giving a value of 2457 Mpc^3 . To-

¹<http://heasarc.gsfc.nasa.gov/docs/rosat/roskof.html>

gether, the upper limit to the number of observable AGNs in our volume becomes ~ 0.17 . This will be an upper limit estimate because the lower redshift bin luminosity functions all seem to level out at lower luminosities, and we assume a constant slope. Hence we should not expect to see any AGNs with the luminosity limits we are constrained with, which also verifies our non-detections.

Infrared results

There is not much to say about the result in infrared, rather than that we got an upper limit to the magnitudes of the sources. We have multiple exposures in each band, because ISAAC can not cover the area spanned by the Ly α sources. Each exposure has a different limiting magnitude but we can conclude the results as an average over the exposures \pm the spread of the limits. In the H band, the limiting magnitude to get a S/N = 2 detection, is $\sim 24.01 \pm 0.24$. Correspondingly in the J and K bands, the limiting magnitudes are $\sim 23.89 \pm 0.15$ and $\sim 23.88 \pm 0.37$. Two of the sources were outside the fields covered by ISAAC, but there is no reason to believe that they would be any different than the ones already investigated.

Conclusions

The first thing to conclude is that the objects found by Fynbo *et al.* (2003) are indeed very faint objects, with a faint continuum of magnitude ~ 27 . The combined results of the flux measurements can be summarised in Table 4.

Table 4	
Summary of results	
Restframe energy	Result ($\text{erg} \cdot \text{s}^{-1}$)
X-rays (1.26 - 33.6 keV)	$L_x < 8.74 \cdot 10^{42}$
B-band (1023 Å)	$\langle L_B \rangle = 8.10 \cdot 10^{42}$
Ly α (1216 Å)	$\langle L_{Ly\alpha} \rangle = 2.91 \cdot 10^{42}$
V-band (1406 Å)	$\langle L_V \rangle = 1.34 \cdot 10^{43}$
I-band (1849 Å)	$\langle L_I \rangle = 7.98 \cdot 10^{42}$
Z-band (2249 Å)	$\langle L_Z \rangle = 3.96 \cdot 10^{42}$
J-band (2976 Å)	$L_J \lesssim 5.85 \cdot 10^{43}$
H-band (3929 Å)	$L_H \lesssim 3.15 \cdot 10^{43}$
K-band (5143 Å)	$L_K \lesssim 1.94 \cdot 10^{43}$

In the table, the $\langle \rangle$ represent the average over the 15 sources. The results on SFR has been to confine it to be greater than a few (and less than two thousand) solar masses per year.

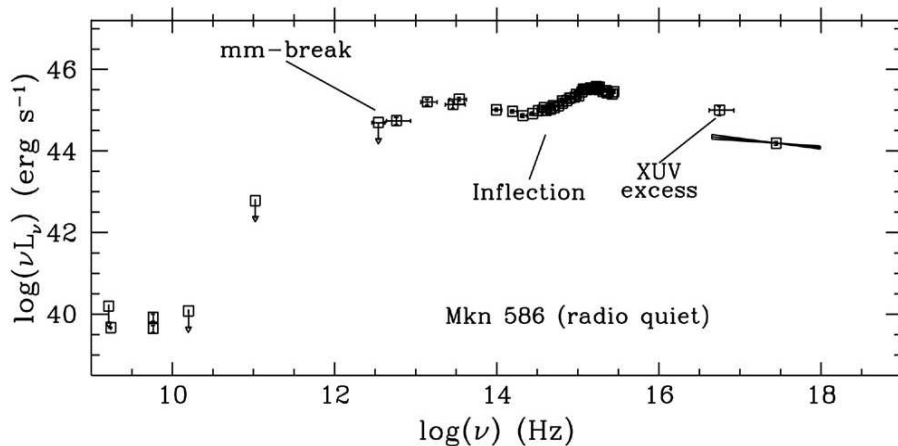


Figure 4.2: Example of AGN spectral energy distribution. From Elvis *et al.* (1994).

Plots of each source spectral energy distribution, SED, were made and can be found in appendix A. A reference example of a radio-quiet AGN spectral energy distribution can be found in Fig. 4.2. In the appendix, the Ly α line is represented by the narrow feature at $\log(\nu) = 15.4$ Hz and broad-band measurements are represented by stars. The overall appearance of the SEDs are that they are similar to the AGN example in Fig. 4.2, but less luminous. The broad band observations, represented by open stars in appendix A, follow a smooth curve, peaking in the V or I band, in most sources. Since this peak lies in UV in the restframe, most of the light must be coming from young O and B stars. It also shows that the light is mostly unobscured from dust, since the effect of dust is to reduce the UV-luminosity. This speaks against a possible Type 2 AGN origin of the X-ray luminosity.

The Ly α -“blob” (Source # 9) was not observed to any significance in X-rays or infrared. It was also very faint in Ly α and broad band measurements. This could be a result of its extension. It is an interesting object that deserves more attention in future observations.

So far, several arguments have been stated as reasons to why we do not detect the sources in the *Chandra* images; the luminosity function calculation giving only 0.17 AGNs in our volume, the hardness ratio being very hard implying highly obscured AGNs (and hence with low luminosity) but the SEDs peaking in UV implying no dust obscuration and no radio counterparts. At least these are reasons against seeing AGNs, and ordinary galaxies have even lower luminosities and will definitely not be seen with our limits to sensitivity. In a very recent paper by Wang *et*

al. (2004), they find similar results. They have studied 101 Ly α emitters at redshift $z \sim 4.5$ with *Chandra* and detect none down to S/N = 3 limits. Stacking the images, with still no detection, gave them a limit to the average luminosity of the sources of $L_{2-8\text{keV}} < 2.8 \cdot 10^{42} \text{ erg s}^{-1}$. The Ly α emitters they observe have very large line equivalent widths, which can be explained by a very young population of stars, or type 2 AGNs. Their main objective with the X-ray investigation is therefore to draw conclusions about the population of type 2 AGNs at that redshift. They compare X-ray to Ly α ratios and find that less than 5 % of their sample can be AGN, a fraction consistent with that in Lyman-break galaxies. The relevance to this thesis is that it is yet another reason to expect no contamination of AGNs among our sources, and therefore an explanation to the non-detections in X-rays.

The future

To complete the survey of these highly interesting sources, further observations with/from the HST in order to study the detailed morphology of the sources and rest-frame UV emission are planned and also observations with the Spitzer satellite (formerly known as SIRTf). The Spitzer satellite sensitivity ranges between 3.6 - 24 μm and observations in this range will constrain the amount of dust in the galaxies. One could also continue working on the SEDs, and try to fit theoretical galaxy spectra to get more information about the galaxies, such as age. Another improvement to the results would be to find more of these Ly α sources to get a greater statistical sample.

Of course, deeper observations with the instruments mentioned throughout this thesis, mainly CXO and ISAAC, would be appreciated. However, if we assume that we would like to reach a sensitivity of $10^{40} \text{ erg s}^{-1}$ for our sources, and we got to a sensitivity of $10^{43} \text{ erg s}^{-1}$ in 1 Ms, then we would need 1 Ts ($1 \cdot 10^{12} \text{ s}$) of exposure time, since the S/N improves as the square-root of the exposure time. 1 Ts corresponds to almost 3200 years which is obviously not possible, and we can only await future observatories with improved detectors.

Chapter 5

Summary

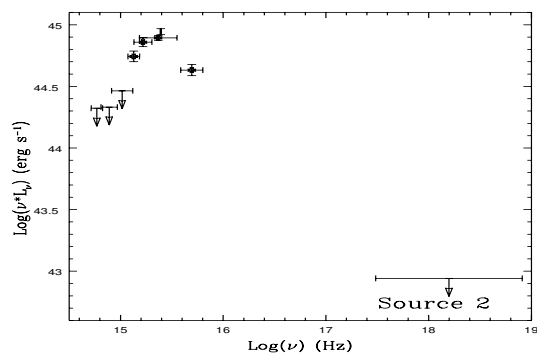
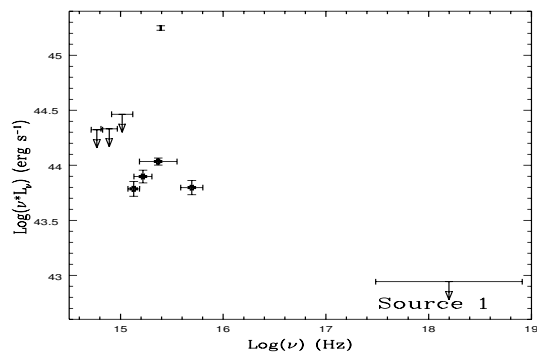
The purpose here was to perform a multi-wavelength analysis of 15 bright Ly α galaxies, and to find the star formation rate of these galaxies. The discovery of the 15 sources was performed before the beginning of this thesis. The sources overlapped the Chandra Deep Field South, CDFS, and a thorough investigation of the Ly α galaxies' X-ray luminosity (in 0.3 - 8 keV) was performed. The results could only set an upper limit to the sources at $\sim 9 \cdot 10^{42}$ erg s $^{-1}$, implying an upper limit of the SFR of 2000 M $_{\odot}$ /yr. This luminosity corresponds to a lower limit to the mass of a central black hole in an AGN of $7 \cdot 10^4$ M $_{\odot}$. Simulations of the luminosity at high redshift were attempted, but as they were based on a theory assuming that all the X-rays came from X-ray binaries, they were not useful. A stacking of the sources with greatest S/N revealed a possible hardness ratio of 0.42, indicating that they are highly obscured AGN (Type 2) if they are detected with such a high luminosity.

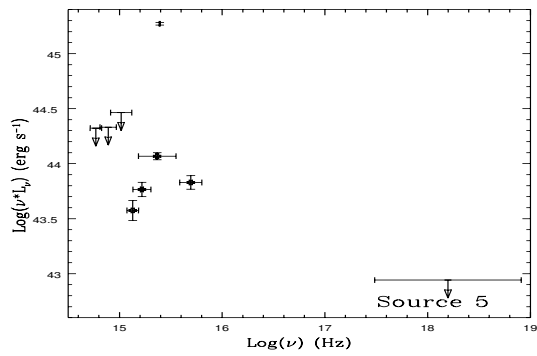
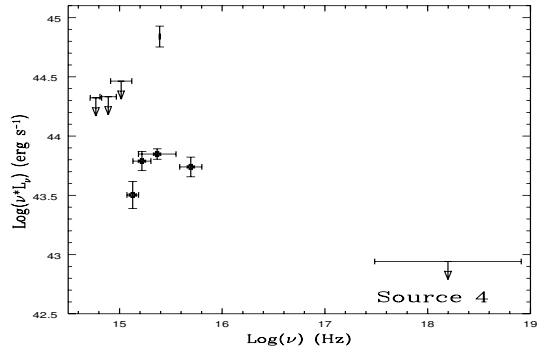
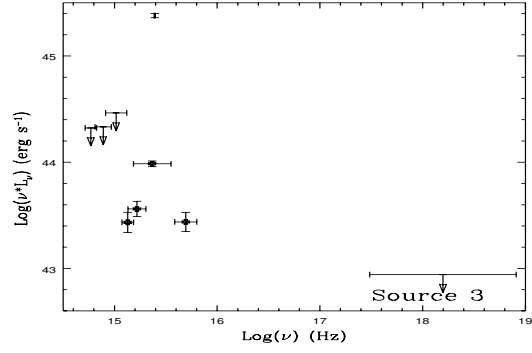
Further investigations were performed in infrared using the ISAAC observations in the GOODS field in the H, J and K bands. The results again only gave an upper limit to the magnitudes of the objects. An investigation of the objects in visual broad bands was performed by Msc-student Brian Krog at Århus university and the results are included in this thesis to give an overall summary of the multi-wavelength properties of the sources. No credible radio counterparts were found in database searches. The luminosity of the sources in the Ly α emission line implied a lower limit of the SFR of a few solar masses per year.

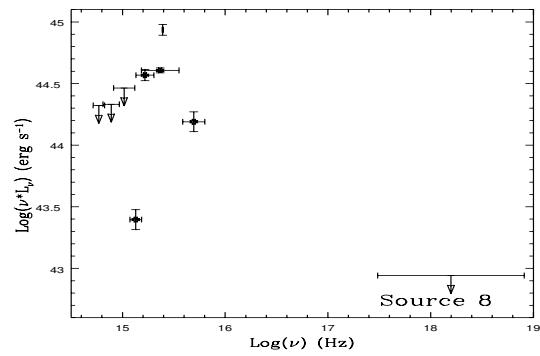
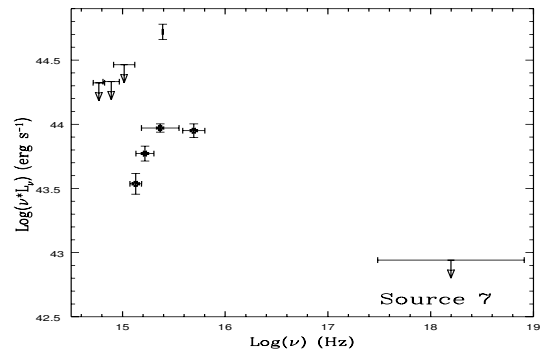
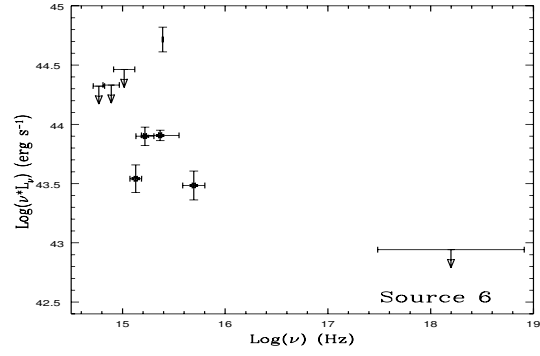
A luminosity function for AGNs in soft X-rays was studied and it was found that there should be 0.17 AGNs in our volume, at our redshift and to our luminosity limit. After comparison to a recent paper by Wang *et al.* (2004) and studying of the results we find that the main conclusion is that there are no AGNs in our sample.

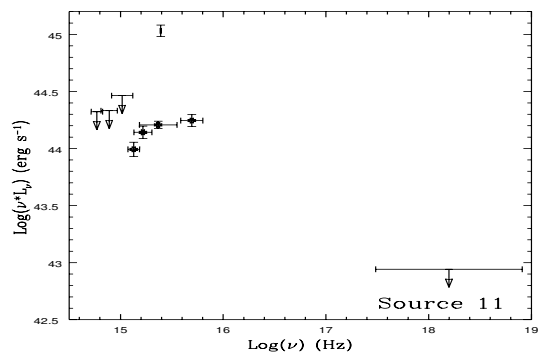
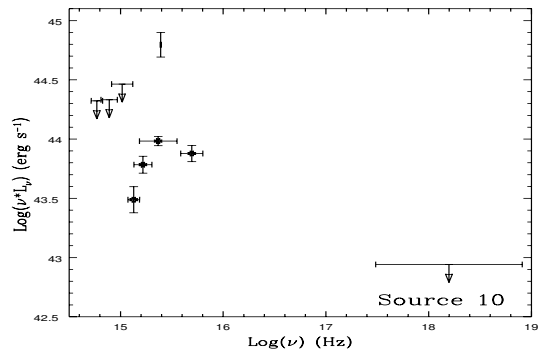
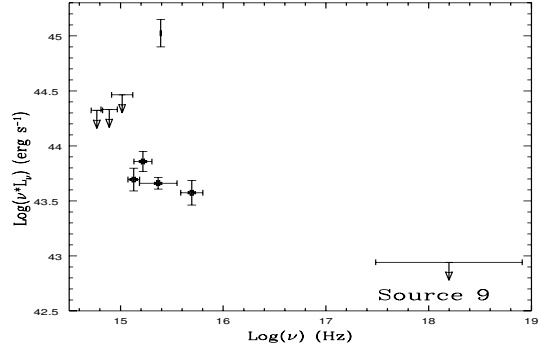
Appendix A

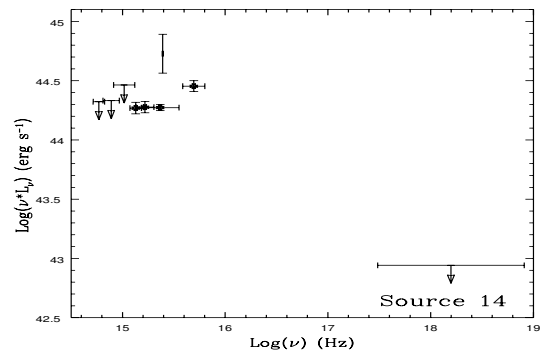
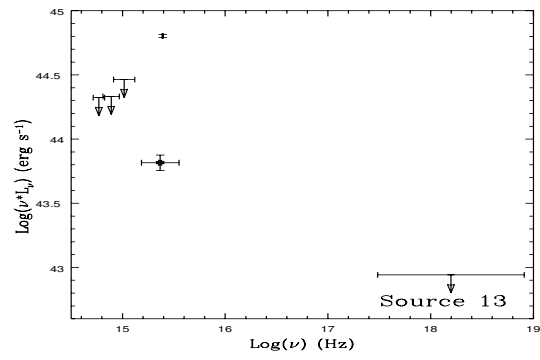
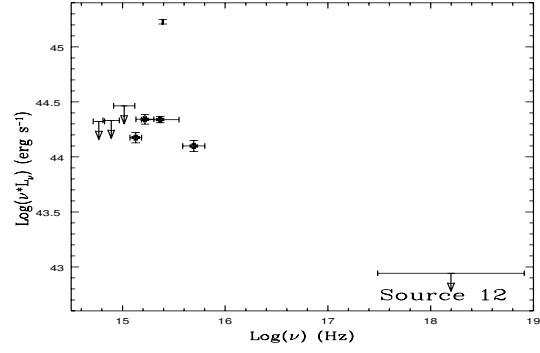
Spectral Energy Distributions

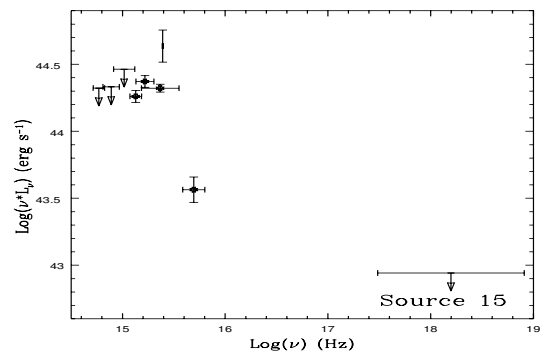












Bibliography

- Blain A.W., Smail I., Ivison R.J., Kneib J.-P., 1999, MNRAS 302, 632
- Brocklehurst M., 1971, MNRAS 153, 471
- Charles P.A., Seward F.D., 1995, Exploring the X-ray universe, Cambridge University Press
- Charlot S., Fall S.M., 1993, ApJ 415, 580
- Chokshi A., 1997, ApJ 491, 78
- Condon J.J., 1992, ARAA 30, 575
- Condon J.J., Cotton W.D., Greisen E.W. *et al.*, 1998, AJ 115, 1693
- Elvis M., Wilkes B.J., McDowell J.C. *et al.*, 1994, ApJS 95, 1
- Fabbiano G., Baldi A., King A.R. *et al.*, 2004, ApJ 605:L21
- Fernandes R.C., Heckman T., Schmitt H., González Delgado R.M., Storchi-Bergmann T., 2001, ApJ 558, 81
- Freeman P.E., Kashyap V., Rosner R., Lamb D.Q., 2002, APJS 138, 185
- Fynbo J.P.U, Ledoux C., Møller P., Thomsen B., Burud I., 2003, A&A 407, 147
- Gandhi P., Crawford C.S., Fabian A.C., Johnstone R.M., 2004, MNRAS 348, 529
- Ghosh P., White N.E., 2001, ApJ 559:L97
- Giacconi R., Rosati P., Tozzi P. *et al.*, 2001, ApJ 551, 624
- Ivison R.J., Greve T.R., Smail I. *et al.*, 2002, MNRAS 337, 1
- Kaaret P., 2002, ApJ 578, 114
- Kennicutt R.C., 1983, ApJ 272, 54
- Madau P., Ferguson H.C., Dickinson M.E. *et al.*, 1996, MNRAS 283, 1388
- Miyaji T., Hasinger G., Schmidt M., 2000, A&A 353, 25
- Mushotzky R.F., Done C., Pounds K.A. and references therein, 1993, ARAA 31, 717
- Norman C., Ptak A., Hornschemeier A., *et al.*, 2004, ApJ 607, 721
- Ohyama Y., Taniguchi Y., Kawabata K.S. *et al.*, 2003, ApJ 591:L9

- Pelló R., Schaerer D., Richard J., Le Borgne J.-F., Kneib J.-P., 2004, *A&A* 416:L35
- Peterson B.M., 1997, *An introduction to active galactic nuclei*, Cambridge University Press
- Ranalli P., Comastri A., Setti G., 2003, *A&A* 399, 39
- Rasmussen J., Sommer-Larsen J., Toft S., Pedersen K., 2004, *MNRAS* 349, 255
- Reddy N.A., Steidel C.C., 2004, *ApJ* 603:L13
- Rosati P., Tozzi P., Giacconi R., *et al.*, 2002, *ApJ* 566, 667
- Ryden B., 2003, *Introduction to cosmology*, Addison Wesley
- Smail I., 2002, *RSPTA* 360, 2697
- Steidel C.C., Adelberger K.L., Shapley A.E. *et al.*, 2003, *ApJ* 592, 728
- Steidel C.C., Adelberger K.L., Shapley A.E. *et al.*, 2000, *ApJ* 532, 170
- Supper R., Hasinger G., Pietsch W. *et al.*, 1997, *A&A* 317, 328
- Urry C.M. and Padovani P., 1995, *PASP* 107, 803
- Wang J.X., Rhoads J.E., Malhotra S. *et al.*, 2004, *ApJ* 608:L21
- Zheng W., Kriss G.A., Telfer R.C., Grimes J.P., Davidsen A.F., 1997, *ApJ* 475, 469

Acknowledgements

I would like to thank all of my supervisors for their help and encouragement. A special thanks for your patience with communication problems, such as long distance. I want to thank “Stiftelsen Malmö Stads Jubileumsfond” for giving me a travel grant for my trips to Copenhagen. I would also like to thank my room-mate at Lund Observatory, Fredrik Svensson, for all the times when my computer and I did not speak the same language and you interpreted and for always being cheerful. And of course, last but not least, a large thank you to my mother who supports me in every possible way I could wish for.